JACS Au
AN OPEN ACCESS JOURNAL OF THE AMERICAN CHEMICAL SOCIETY

pubs.acs.org/jacsau
Article

Biomimetic Vesicles with Designer Phospholipids Can Sense Environmental Redox Cues

Huseyin Erguven,[▽] Liming Wang,[▽] Bryan Gutierrez, Andrew H. Beaven, Alexander J. Sodt, and Enver Cagri Izgu*

Cite This: *JACS Au* 2024, 4, 1841−1853

ABSTRACT: Cell-like materials that sense environmental cues can serve as next-generation biosensors and help advance the understanding of intercellular communication. Currently, bottom-up engineering of protocell models from molecular building blocks remains a grand challenge chemists face. Herein, we describe giant unilamellar vesicles (GUVs) with biomimetic lipid membranes capable of sensing environmental redox cues. The GUVs employ activity-based sensing through designer phospholipids that are fluorescently activated in response to specific reductive (hydrogen sulfide) or oxidative (hydrogen peroxide) conditions. These synthetic phospholipids are derived from 1,2-dipalmitoyl-*rac*-glycero-3-phosphocholine and they possess a headgroup with heterocyclic aromatic motifs. Despite their structural deviation from the phosphocholine headgroup, the designer phospholipids (0.5−1.0 mol %) mixed with natural lipids can vesiculate, and the resulting GUVs (7−20 μm in diameter) remain intact over the course of redox sensing. All-atom molecular dynamics simulations gave insight into how these lipids are positioned within the hydrophobic core of the membrane bilayer and at the membrane−water interface. This work provides a purely chemical method to investigate potential redox signaling and opens up new design opportunities for soft materials that mimic protocells.

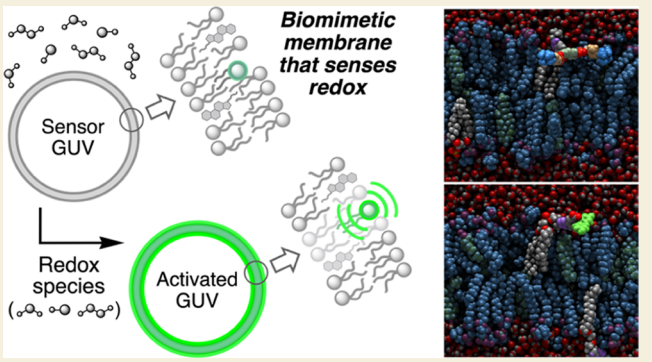

KEYWORDS: *cell-like materials, giant unilamellar vesicle, signaling, biosensing, redox, lipid membrane, MD simulation*

Cell-like supramolecular assemblies, protocell models, and semisynthetic organisms can be employed for studying origins of cellular life,[1] membrane biogenesis and regulation,[2] cell development,[3] differentiation,[4] and signaling,[5] for producing biofuel,[6,7] or hormones[8], for detecting metabolites,[9] pathogens,[10] or agricultural pollutants,[11] and for building cytomimetic tissues in regenerative medicine,[12] and targeted drug delivery.[13,14]

A central goal in building cell-like materials is to configure the minimal requirements for cellular processes, which include, among others, sensing "extracellular" environment.[15] Much of the focus in building protocell-based sensors has been on compartmentalizing enzymes and well-defined genetic networks,[4,16−20] while activity-based sensing through functional amphiphiles localized in membranous compartments has been overlooked. This is at odds with the surging interest in synthetic lipids and the demand for applying them in research geared toward biosensing, cellular imaging, and optical control of biological processes.[21−26] Lipid modifications can indeed offer protocell designs with programmable functions or with features that are naturally inaccessible.[27−30] However, implementing synthetic amphiphiles to construct a membranous compartment capable of sensing its environment while maintaining its biophysical integrity is a technical bottleneck, especially given that we know little about how unnatural lipids behave in membranes. In accordance, we focused our attention on synthetic organic chemistry principles to construct giant unilamellar vesicles (GUVs) with programmable membrane functions. GUVs are widely used as protocell models[31,32] because they have physical characteristics feasible to visualize by light microscopy and relevant to those of eukaryotic cells, such as dimension (1−30 μm in diameter) and membrane mechanics.[33−35] One of the GUV functions we are interested in achieving using synthetic tools and chemical principles is to configure biomimetic membranes that sense cues important for redox biochemistry and cell signaling (Figure 1).

Real-time detection of redox species in proximity to a lipid vesicle could give insight into their interactions with and diffusivity across bilayer membranes, which are critical

Received: January 9, 2024
Revised: March 6, 2024
Accepted: March 26, 2024
Published: April 15, 2024

https://doi.org/10.1021/jacsau.4c00041
JACS Au 2024, 4, 1841−1853

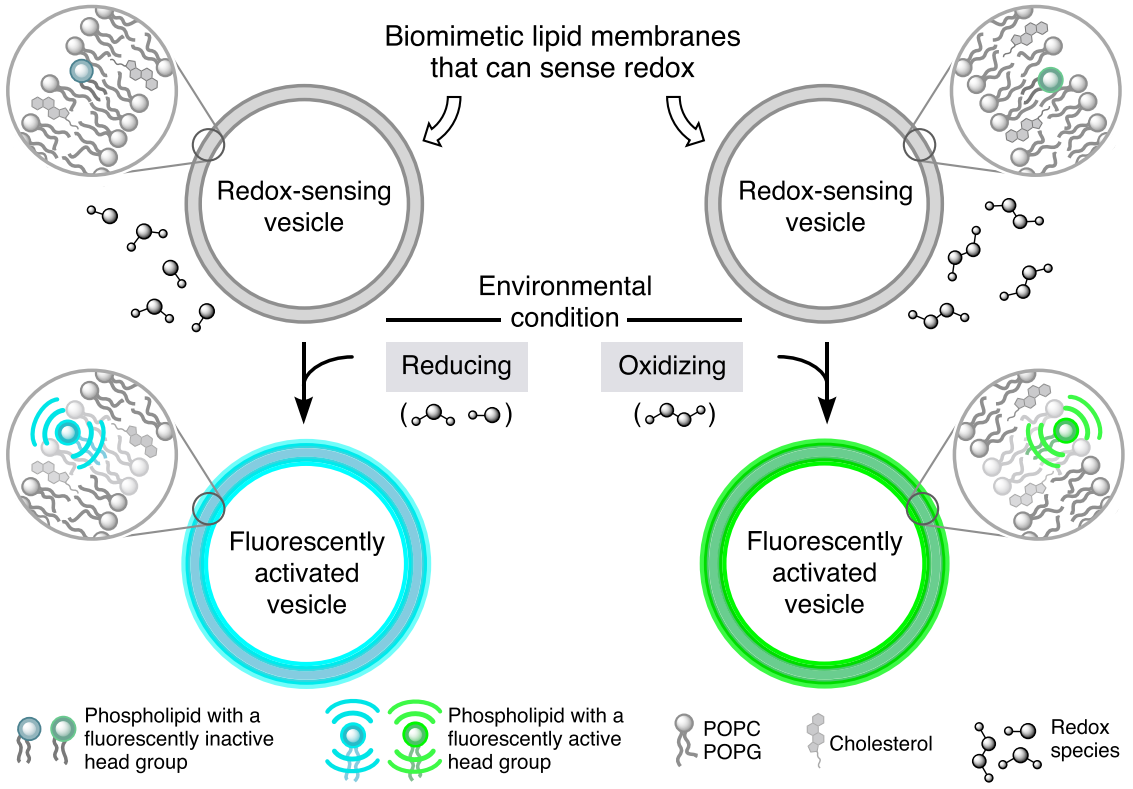

Figure 1. Overview of redox sensors built from biomimetic lipid membranes. Each membrane system contains a mixture of natural lipids (POPC, POPG, and cholesterol) and a synthetic lipid that specifically reacts with a target redox species.

physiochemical factors for intercellular signaling.[36−38] Hydrogen sulfide (H_2S), a reactive sulfur species (RSS), and hydrogen peroxide (H_2O_2), a reactive oxygen species (ROS), are two redox molecules with significant roles in diverse biological processes, ranging from signal transduction to pathophysiology.[38−42] There has been an increasing degree of appreciation for both H_2S and H_2O_2 due to their roles in cellular communication, and the underlying mechanisms of how they modulate signaling are the focus of evolving research.[43,44] H_2S serves as a gasotransmitter in mammals[38] and is involved in signal transduction pathways pertaining to neurological[45−47] and cardiovascular[48,49] functions. Typically, it diffuses through lipid membranes without specialized channels.[50] H_2O_2 serves in a number of diverse biological processes from signal transduction[41] to cell differentiation and proliferation.[51] H_2O_2 transport across membranes occurs through simple diffusion or is facilitated by aquaporins.[52,53]

In this work, we describe the development, application, and atomistic molecular dynamics (MD) simulations of biomimetic membranes that fluoresce in response to reducing or oxidizing conditions (Figure 1). These membranes employ designer phospholipids **DPPC-TC-H_2S** and **DPPC-TF-H_2O_2** (Scheme 1), each possessing the 1,2-dipalmitoyl-*rac*-glycero-3-phosphocholine (*rac*-DPPC) amphiphilic framework and an inactivated fluorogen that is sensitive to redox. We utilized **DPPC-TC-H_2S** or **DPPC-TF-H_2O_2** (0.5−1.0 mol %), along with 1-palmitoyl-2-oleoyl-*sn*-glycero-3-phosphocholine (POPC), 1-palmitoyl-2-oleoyl-*sn*-glycero-3-(phosphor-*rac*-(1-glycerol)) (POPG), and cholesterol, to construct GUVs that sense either H_2S or H_2O_2. Based on confocal imaging, the vesicles remained intact after the redox-induced chemical transformation of designer phospholipids, which exemplifies a biomimetic membrane system with potential for studying biological membranes.[54] All-atom MD simulations demonstrated that the designer lipids with natural hydrocarbon tails can reside in bilayers, with their headgroups fluctuating between the membrane core and bulk water.

RESULTS AND DISCUSSION

Phospholipids that Sense Redox Have Modular Chemical Designs

Both **DPPC-TC-H_2S** and **DPPC-TF-H_2O_2** possess a modular design, in which the redox-sensing group, a caged coumarin or fluorescein, is connected to *rac*-DPPC through a triazole ring (Scheme 1). The choice of using a fully saturated phospholipid stemmed from the availability of its building block (1,2-dipalmitoyl-*rac*-glycerol) at synthetically feasible costs and scales. To facilitate quantitative investigations of the redox-mediated fluorescence activation mechanism, kinetics, and fidelity, we synthesized the hydrophilic analogs **TEG-TC-H_2S** and **TEG-TF-H_2O_2**, which contain a triethylene glycol (TEG) in place of the *rac*-DPPC module to enhance water solubility. These TEG analogs aided our analytical assessments (e.g., mass spectrometry and plate reader measurements) of probes in aqueous buffer without the complication of aggregation.

The syntheses of the probes harnessed alkynyl *rac*-DPPC **1** and readily available propargyl-TEG-OH **2**. We obtained **1** from 1,2-dipalmitoyl-*rac*-glycerol in 54% yield over two steps, using ethylene chlorophosphite, followed by 3-dimethylamino-1-propyne.[55] These alkynes (**1** and **2**) were conjugated with 3-azido-7-hydroxycoumarin (**4**) via a copper-catalyzed azide−alkyne cycloaddition ("click") reaction, affording **DPPC-TC** and **TEG-TC** in 33 and 55% yields, respectively. The 7-*O*-coumarin atom of each click produtc was then benzylated using 4-azidobenzyl bromide (**3**), providing **DPPC-TC-H_2S** and

https://doi.org/10.1021/jacsau.4c00041
JACS Au 2024, 4, 1841−1853

Scheme 1. Chemical Syntheses of the Phospholipid-Based Redox Probes DPPC-TC-H_2S and DPPC-TF-H_2O_2, Along with Their Hydrophilic Analogs TEG-TC-H_2S and TEG-TF-H_2O_2[a]

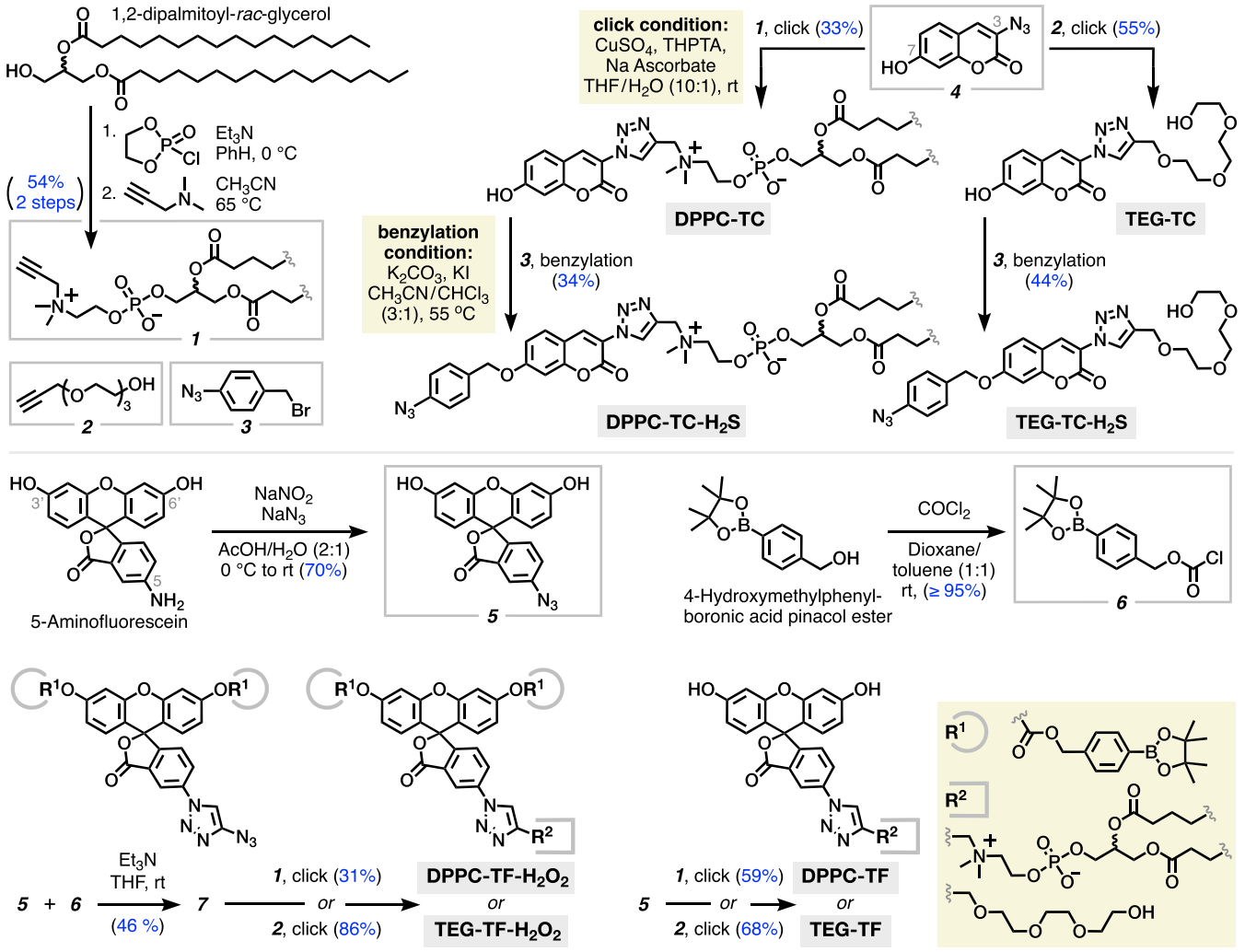

[a]THPTA: tris(3-hydroxypropyltriazolylmethyl)amine. Solvent mixture in click condition toward **TEG-TF**: THF/H_2O (3:1).

TEG-TC-H_2S in 34 and 44% yields, respectively. The H_2O_2 probes **DPPC-TF-H_2O_2** and **TEG-TF-H_2O_2** were synthesized from 5-aminofluorescein in three linear steps. First, 5-aminofluorescein was converted to 5-azidofluorescein (**5**) through diazotization followed by azide treatment. Compound **5** was functionalized at both of its exocyclic xanthene oxygens (3′ and 6′) using compound **6**, the chloroformate obtained from 4-hydroxymethylphenyl-boronic acid pinacol ester. The resulting azido biscarbonate **7** served as a common precursor for both **DPPC-TF-H_2O_2** and **TEG-TF-H_2O_2**. We connected **7** with the alkyne **1** or **2** via the click reaction to obtain **DPPC-TF-H_2O_2** or **TEG-TF-H_2O_2** in 31 or 86% yield, respectively. For fluorescence characterization studies, we separately synthesized their redox products, **DPPC-TF** and **TEG-TF**, directly from the azide **5** and the alkyne **1** or **2** via the click reaction.

Redox Sensing Occurs via Uncaging of the Coumarin or Fluorescein Motif and with Good Selectivity

Currently, there are mixed reports on the physiological concentrations of free H_2S, suggesting that accurate measurements of its concentrations have been challenging.[56] Recently, mammalian cell responses triggered by H_2S, such as angiogenesis of endothelial cells, have been investigated using 10–600 μM exogenous H_2S.[57] Guided by this study, we reasoned that administering 500 μM Na_2S into a pH 7.5 medium (Tris, 5 mM) would generate H_2S at a concentration that falls within the biologically relevant concentration range. At this pH, roughly 20% of the sulfur species is expected to exist in the form of H_2S (~100 μM) as the pK_a of H_2S is ~7.0.[58] Based on a combined experimental and computational investigation, it has been proposed that sulfide-mediated reduction of aryl azides to aryl amines is induced by HS^- as the active sulfur species.[59] Our aryl azide-containing probes, which are named as **DPPC-TC-H_2S** and **TEG-TC-H_2S** by convention, would therefore likely detect an equilibrium mixture of H_2S and HS^- in a physiologically relevant milieu. As for H_2O_2, we sought to employ the concentration conditions under which the biogenesis of H_2O_2 has been investigated through peroxidase kinetics analyses.[60] In accordance with these analyses, the rate of H_2O_2 production from isolated peroxisomes has been estimated to be 90 nmol/min per gram of rodent liver.[60] Furthermore, a concentration range of 10–100 μM is correlated with oxidative stress under physiological conditions based on protein activity assays in human alveolar adenocarcinoma cells.[61] In light of these reports, we used H_2O_2 concentrations of up to 100 μM in the investigations of **TEG-TF-H_2O_2** and **DPPC-TF-H_2O_2**.

https://doi.org/10.1021/jacsau.4c00041
JACS Au 2024, 4, 1841–1853

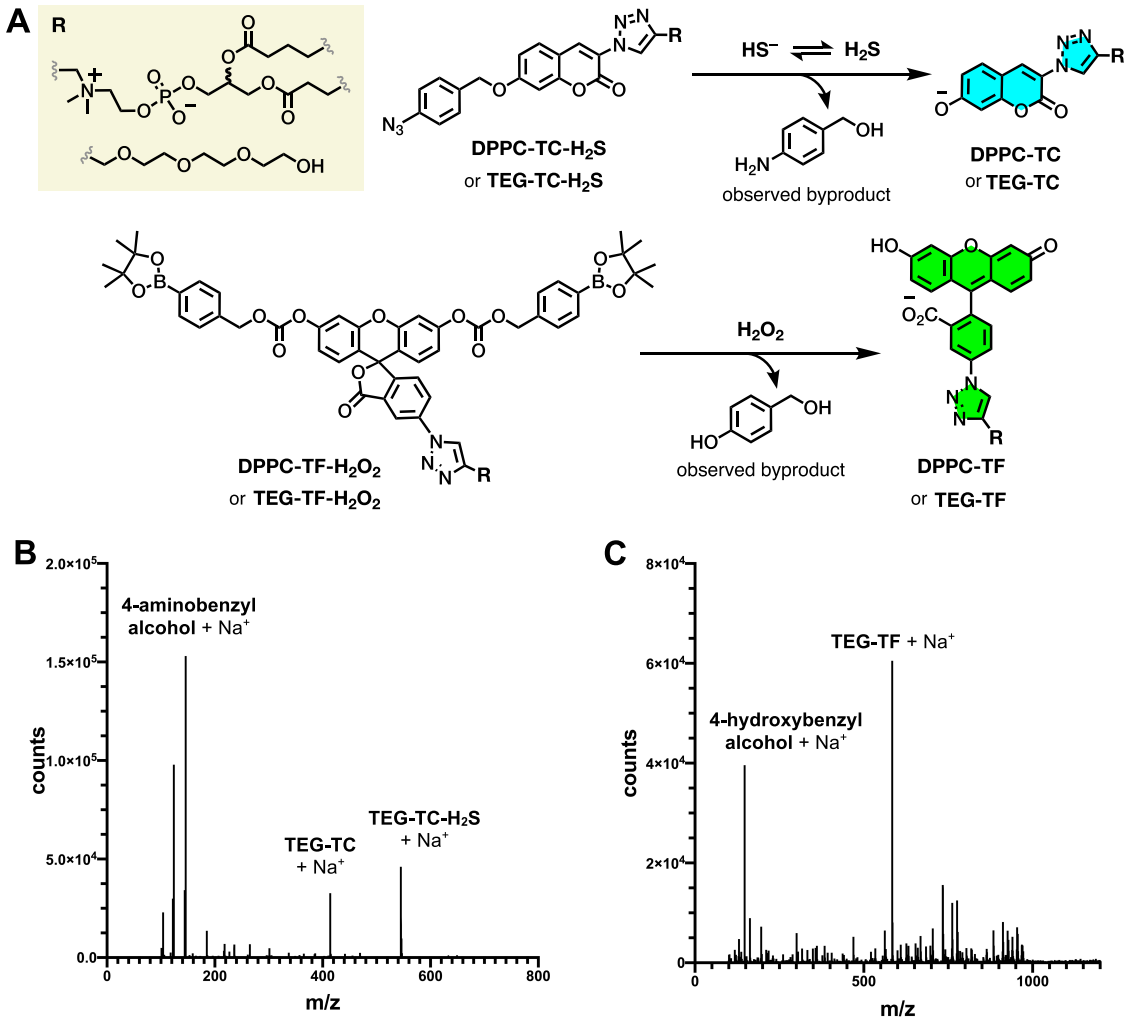

Figure 2. Fluorescence activation of the amphiphilic and hydrophilic redox probes. (A) Chemical transformations of the probes treated with their cognate redox species. DPPC-TF and TEG-TF shown in ring-opened form. (B, C) HRMS analyses of the mixtures initially containing (B) TEG-TC-H_2S and Na_2S and (C) TEG-TF-H_2O_2 and H_2O_2. The spectral data were collected in positive ionization mode and through direct injection of the reaction aliquots taken after (B) 3 h or (C) 1 h. (B) 4-Aminobenzyl alcohol, $[M + Na]^+$, requires 146.0576; found 146.0588; TEG-TC, $[M + Na]^+$, requires 414.1272; found 414.1288; TEG-TC-H_2S, $[M + Na]^+$, requires 545.1755; found 545.1772; (C) 4-hydroxybenzyl alcohol, $[M + Na]^+$, requires 147.0417; found 147.0426; TEG-TF, $[M + Na]^+$, requires 584.1640; found 584.1641. TEG-TF-H_2O_2 *m/z* peak ($[M + Na]^+$, requires 1104.4079) was not observed here, suggesting that its consumption ($[M + Na]^+$ peak is detectable for the isolated compound, see the Supporting Information). Reaction conditions: (B) TEG-TC-H_2S (20 μM), Na_2S (500 μM), and Tris (50 mM, pH 7.5). (C) TEG-TF-H_2O_2 (50 μM), H_2O_2 (100 μM), and Tris (50 mM, pH 7.5).

Table 1. Characterization of the Amphiphilic and Hydrophilic Probes and Their Uncaged Forms

entry	compound	max ex (nm)	max em (nm)	extinction coefficient (M^{-1} cm^{-1})	quantum yield	brightness	relative brightness[a]
1	**TEG-TC-H_2S**	392.3	475.5	5347	0.07	374	5.2
2	**TEG-TC**	397.0	471.4	15 613	0.66	10 305	143.2
3	**DPPC-TC-H_2S**	396.5	473.5	2411	0.03	72	1.0
4	**DPPC-TC**	398.0	472.0	13 749	0.64	8799	122.2
5	**TEG-TF-H_2O_2**	492.0	526.0	13 429	0.04	537	2.5
6	**TEG-TF**	494.3	522.6	35 982	0.73	26 267	122.7
7	**DPPC-TF-H_2O_2**	495.2	519.5	10 685	0.02	214	1.0
8	**DPPC-TF**	498.1	523.6	28 990	0.63	18 264	85.3

[a]Samples were prepared using ethanol. Entries 1, 2, and 4: Brightness compared to that of **DPPC-TC-H_2S** (entry 3). Entries 5, 6, and 8: Brightness compared to that of **DPPC-TF-H_2O_2** (entry 7).

To gain a mechanistic understanding of the redox transformations (Figure 2A), we analyzed the mixtures of probes with their cognate redox species by high-resolution mass spectrometry (HRMS) (Figure 2B,C, Table S1). It is worth noting that the reaction samples containing amphiphilic probes, **DPPC-TC-H_2S** and **DPPC-TF-H_2O_2**, displayed poor electrospray ionization profiles in both positive and negative ion modes. In contrast, their hydrophilic analogs, **TEG-TC-H_2S** and **TEG-TF-**

https://doi.org/10.1021/jacsau.4c00041
JACS Au 2024, 4, 1841−1853

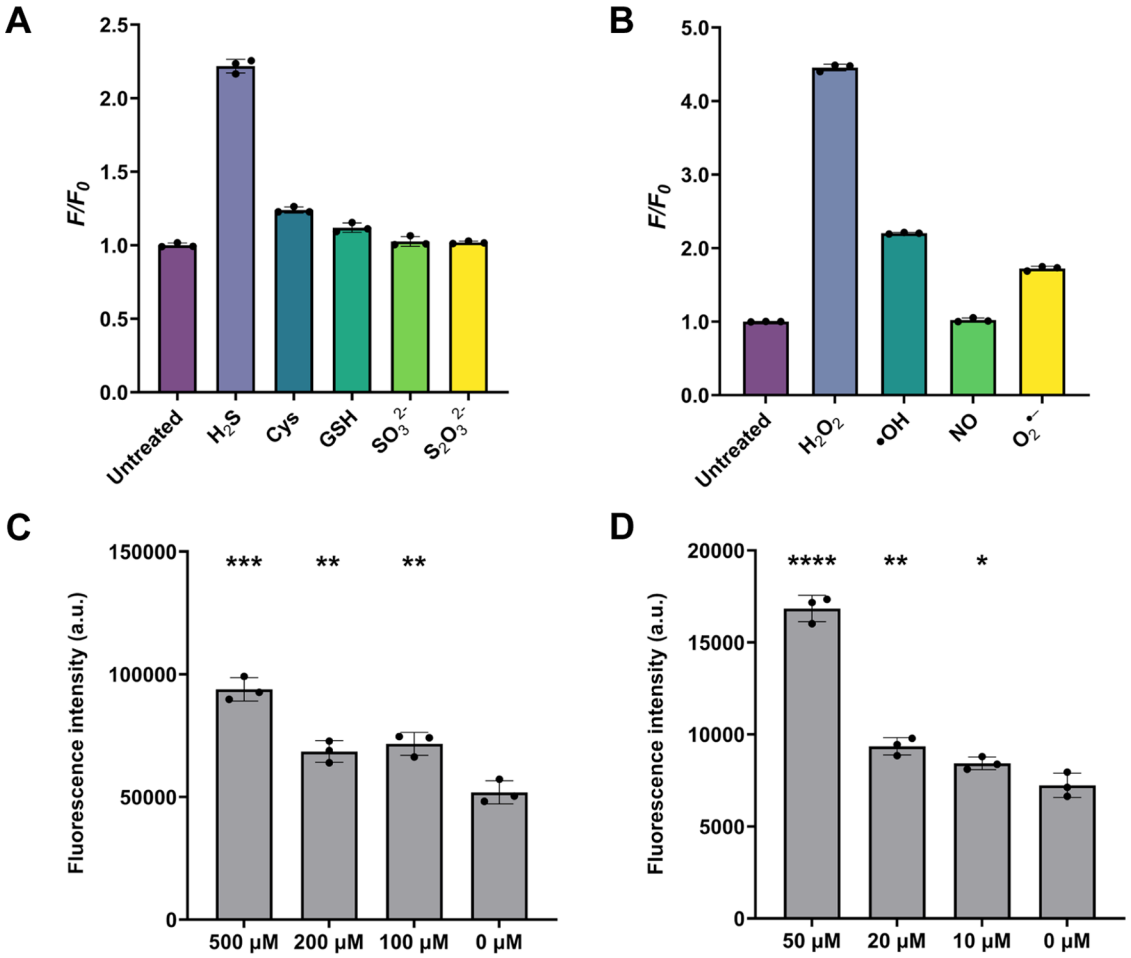

Figure 3. Specificity (A, B) and limit of detection (LoD) (C, D) of TEG-TC-H_2S and TEG-TF-H_2O_2. LoD measurements for the probes TEG-TC-H_2S (390/475 nm) and TEG-TF-H_2O_2 (485/525 nm) were performed in Tris buffer (50 mM, pH 7.5). Error bars represent the standard deviation; n = 3. Single-tailed Student's t-test: *P < 0.05; **P < 0.01; ***P < 0.001; ****P < 0.0001.

H_2O_2, provided evidence for the expected redox transformations with H_2S and H_2O_2, respectively. The aliquot taken from the reaction mixture of **TEG-TC-H_2S** and Na_2S showed 4-aminobenzyl alcohol ($[M + Na]^+$ = 146, Figure 2B), suggesting a 1,6-elimination followed by hydration of the putative elimination byproduct. The aliquot from the solution of **TEG-TF-H_2O_2** incubated with H_2O_2 showed 4-hydroxybenzyl alcohol ($[M + Na]^+$ = 147, Figure 2C), suggesting a similar elimination/hydration cascade triggered by the oxidation of both phenylboronic pinacol esters.

Next, we assessed the impact of caging and uncaging of the coumarin or fluorescein on their fluorogenicity by measuring the relative fluorescence quantum yield (Φ_{Frel}) values (Table 1). We used coumarin 343 as the standard for measuring Φ_{Frel} of the triazole-coumarin compounds (**TEG-TC-H_2S**, **TEG-TC**, **DPPC-TC-H_2S**, and **DPPC-TC**), whereas we used fluorescein for the triazole-fluorescein compounds (**TEG-TF- H_2O_2**, **TEG-TF**, **DPPC-TF-H_2O_2**, and **DPPC-TF**). Relative to coumarin 343, whose absolute fluorescence quantum yield (Φ_F) is 0.63 in ethanol,[62] Φ_{Frel}s of **TEG-TC-H_2S** (entry 1) and **DPPC-TC-H_2S** (entry 3) were determined to be 0.07 and 0.03, respectively. Their O-uncaged forms, **TEG-TC** (entry 2) and **DPPC-TC** (entry 4), exhibited a 10- to 20-fold increase in quantum yield, with ∼30- and 120-fold enhanced brightness, respectively. The pK_a of **TEG-TC** is 7.1 ± 0.1 based on UV−vis spectrophotometric measurements.[55] Under the redox conditions here (Tris 50 mM, pH 7.5), a substantial population of the coumarin should exist in aryloxide anion form ($^-$O-aryl), which is expected to exhibit a stronger fluorescence compared to the neutral form (HO-aryl). Relative to fluorescein, whose Φ_F is 0.79 in ethanol,[63] Φ_{Frel} values of the H_2O_2 probes **TEG-TF-H_2O_2** (entry 5) and **DPPC-TF-H_2O_2** (entry 7) were determined to be 0.04 and 0.02, respectively. Their uncaged forms, **TEG-TF** (entry 6) and **DPPC-TF**, (entry 8) exhibited a 20- to 30-fold increase in quantum yield and 49-fold or higher enhanced brightness. See Figure S1 for the emission spectra of the probes and their uncaged forms. These results validated that caging the coumarin moiety through benzylation of its 7-O atom and caging the fluorescein moiety via carbonylation of its 3′ and 6′-O-xanthene atoms decrease Φ_{Frel} and brightness.

The redox-specificities of the hydrophilic probes, **TEG-TC-H_2S** or **TEG-TF-H_2O_2**, were assessed by subjecting them to various RSS or ROS (Figure 3A,B). Change in fluorescence intensity following excitation of each sample containing the respective probe was measured over 120 min of incubation and presented based on the signal-to-background ratio F/F_0, where F and F_0 are defined as the fluorescence with and without the redox species. The F/F_0 values of the untreated samples were set to 1 for comparisons. In this study, we used higher concentrations of sulfur species due to fluorescence generation rates being somewhat slower than expected. While it is outside the scope of this work, we are interested in exploring ways to

https://doi.org/10.1021/jacsau.4c00041
JACS Au 2024, 4, 1841−1853

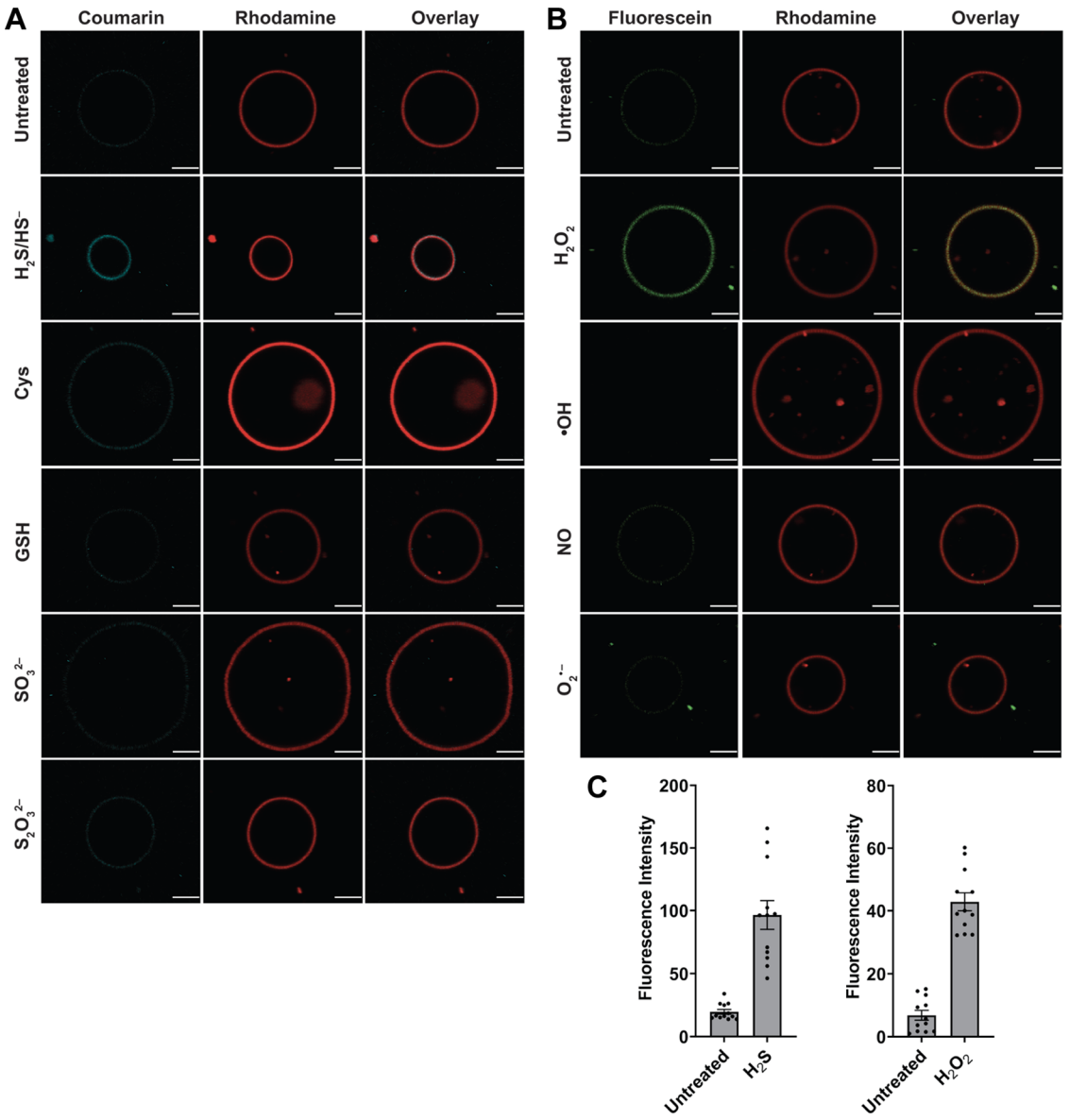

Figure 4. GUVs that can sense (A) reductive or (B) oxidative environments. Confocal images acquired for the (A) HS^-/H_2S-sensing GUVs at 405:475 nm (ex/em) and (B) H_2O_2-sensing GUVs at 490:520 nm. Lipid compositions of GUVs: (A) POPC, POPG, cholesterol, and DPPC-TC-H_2S (48:21:30:1 molar ratio); (B) POPC, POPG, cholesterol, and DPPC-TF-H_2O_2 (48.5:21:30:0.5 molar ratio). To label vesicle membranes, Liss-Rhod PE dye (ex/em channel: 560:610 nm) was introduced to the lipid mixture at an insignificant molar ratio (0.1 mol %). Initial concentrations of RSS and ROS were set to 500 and 100 μM, respectively. Scale bar = 5 μm. (C) Quantitative assessment of fluorescence signals from vesicle membranes. Error bars represent the standard error of the mean (SEM).

speed up the reduction process and will report our findings in due course. Upon addition of Na_2S (1 mM estimated initial H_2S concentration), the sample containing **TEG-TC-H_2S** exhibited a steady increase in fluorescence intensity over 2 h of incubation, reaching 2.2-fold fluorescence compared to the sample untreated (Figure 3A). The sample containing **TEG-TF-H_2O_2** and treated with 100 μM H_2O_2 presented a steady fluorescence enhancement within 2 h, resulting in 4.4-fold higher fluorescence than that of the untreated sample (Figure 3B). Interestingly, the untreated sample showed a spontaneous increase in fluorescence over the course of 2 h, suggesting that a small quantity of **TEG-TF-H_2O_2** was possibly being hydrolyzed at pH 7.5.

We evaluated the selectivity of these hydrophilic probes against nontarget RSS and ROS. **TEG-TC-H_2S** was subjected to cysteine (Cys), glutathione (GSH), sulfite (SO_3^{2-}), and thiosulfate ($S_2O_3^{2-}$). At 1 mM initial concentration and for a total incubation time of 2 h, these sulfur species induced an increase in coumarin fluorescence by less than 25% compared to the untreated sample (Figure 3A). The measurements indicated that **TEG-TC-H_2S** undergoes fluorescence activation by a degree of 5-fold or more in the presence of H_2S, which induced a 120% increase in fluorescence intensity, compared to the other RSS. The specificity of **TEG-TF-H_2O_2** toward H_2O_2 was assessed against 100 μM hydroxyl radical ($^{\bullet}OH$), nitric oxide ($^{\bullet}NO$), or superoxide radical ($O_2^{\bullet-}$). Among these three reactive oxygen species, $^{\bullet}OH$ induced the highest fluorescence increase (2.2-fold), which was still lower than that for H_2O_2 (4.4-fold). The relatively low yet observable reactivity of $^{\bullet}OH$ may have been due, in large part, to the residual unreacted H_2O_2 used for generating $^{\bullet}OH$.[64]

https://doi.org/10.1021/jacsau.4c00041
JACS Au 2024, 4, 1841−1853

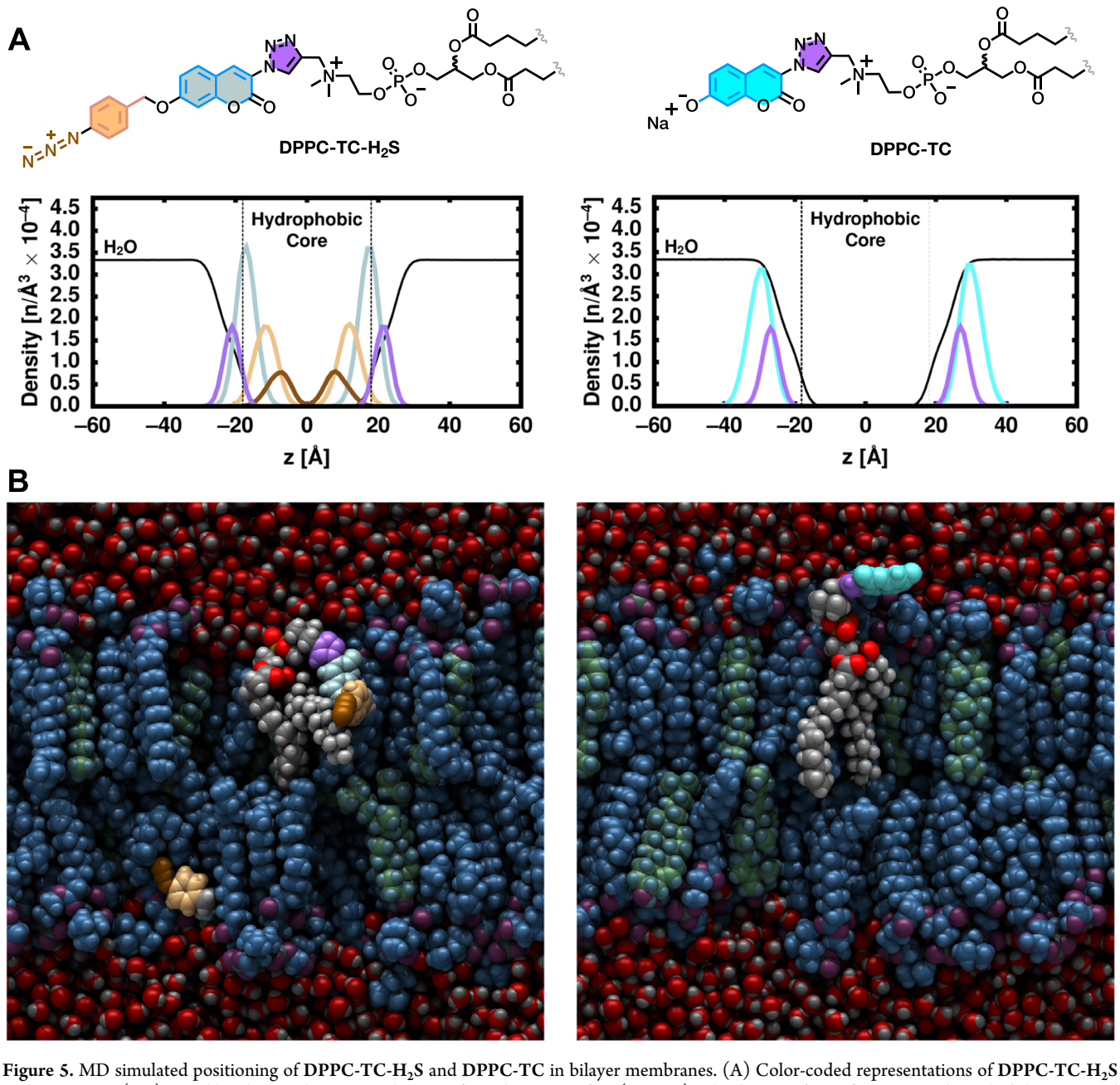

Figure 5. MD simulated positioning of **DPPC-TC-H_2S** and **DPPC-TC** in bilayer membranes. (A) Color-coded representations of **DPPC-TC-H_2S** and **DPPC-TC** (top). Lipid headgroup densities in the water/membrane interface (bottom). The density of specific moieties along the bilayer normal (z) calculated with 1 Å bins. The water density is scaled down by 100x to be on a similar scale as the moiety densities (TIP3P water has a bulk density of ~0.0333 molecules/Å^3). The dotted vertical lines indicate the hydrophobic core of the bilayer defined as the region between the acyl chain carbonyl groups. (B) Snapshots of the simulated water−membrane interface taken from 2 μs time point. Left image: Bilayer containing **DPPC-TC-H_2S**. Right image: Bilayer with **DPPC-TC**.

LoD for each probe was determined by evaluating the statistical differences between F and F_0 at varying concentrations of H_2S or H_2O_2, where F and F_0 are the fluorescence intensities with and without the corresponding redox-active species. Here, LoD is defined as the minimum redox species concentration at which F is higher than F_0 using the one-tailed Student's t-test. The LoD of **TEG-TC-H_2S** was determined as 100 μM (Figure 3C), and the LoD of **TEG-TF-H_2O_2** was determined as 10 μM (Figure 3D).

GUVs Respond to Either Hydrogen Sulfide or Hydrogen Peroxide

In most biomimetic systems that rely on compartmentalization, eukaryotic membrane boundaries are often modeled using GUVs comprised of phospholipids and cholesterol.[34]

We produced GUVs from a mixture of POPC, POPG, cholesterol, and the DPPC-derived probe (~48:21:30:0.5−1.0 molar ratio) using electroformation[65] and imaged the resulting vesicles via confocal microscopy (Figure 4). To locate vesicle membranes prior to redox treatment and to assess whether the lipid redox products (**DPPC-TC** and **DPPC-TF**) remain within the bilayers, we used the fluorescent membrane dye 1,2-dioleoyl-*sn*-glycero-3-phosphoethanolamine-*N*-(lissamine rhodamine B

https://doi.org/10.1021/jacsau.4c00041
JACS Au 2024, 4, 1841−1853

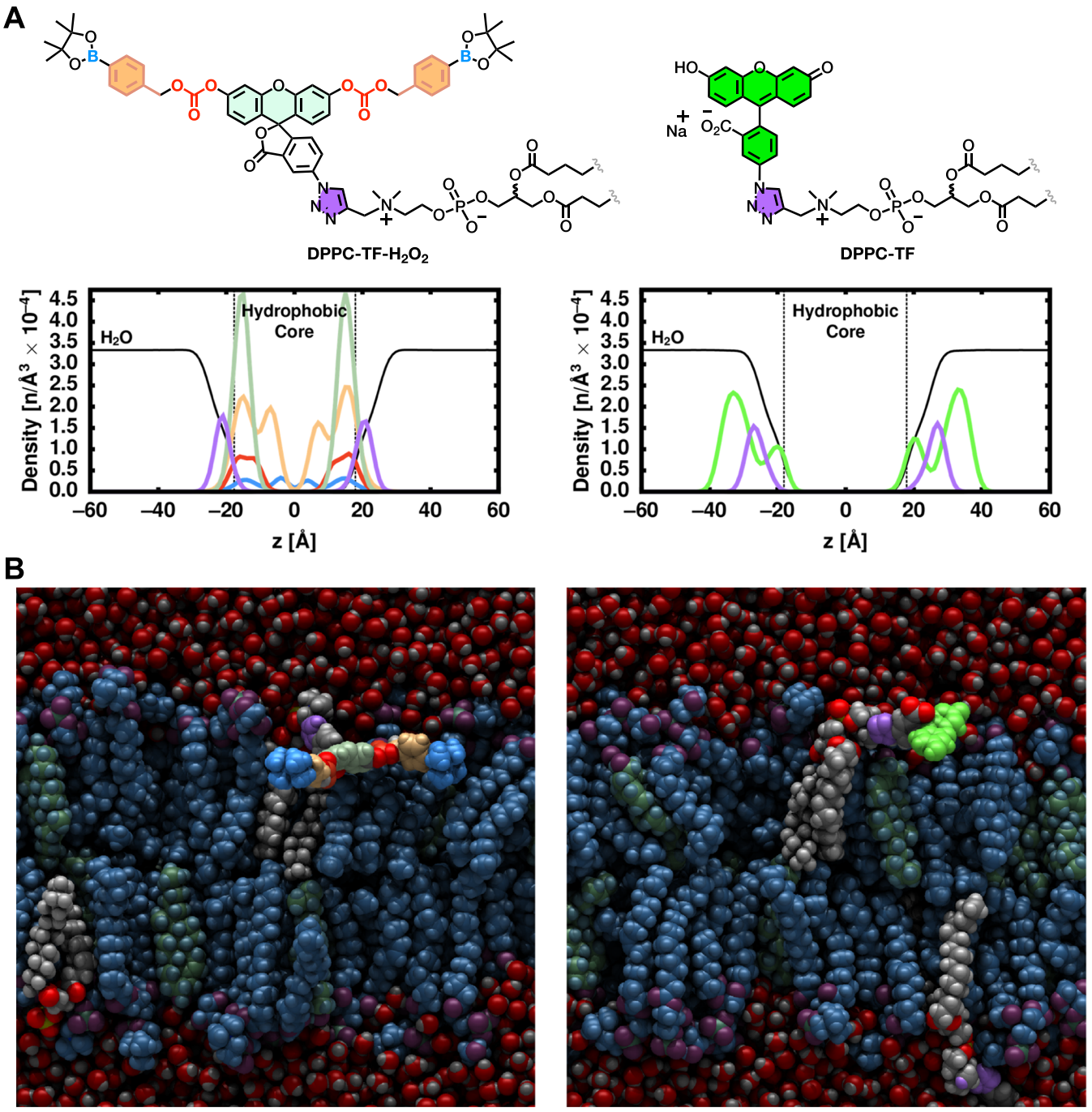

Figure 6. MD simulated positioning of **DPPC-TF-H_2O_2** and **DPPC-TF** in bilayer membranes. (A) Color-coded representations of **DPPC-TF-H_2O_2** and **DPPC-TF** (top). Lipid headgroup densities in water/membrane interface (bottom). The parameters used for the plots are the same as those described in Figure 5. (B) Snapshots of the simulated water−membrane interface taken from 2 μs time point. Left image: Bilayer containing **DPPC-TF-H_2O_2**. Right image: Bilayer with **DPPC-TF**.

sulfonyl) (18:1 Liss-Rhod PE) at 0.1 mol % of the total lipid composition. Solutions of the lipids in organic solvents (chloroform with or without methanol) were mixed and concentrated to a thin film, which was then hydrated with sucrose (300 mM) and Tris (5 mM) at pH 7.5. Using this relatively high sucrose concentration was critical for the formation of GUVs, which can be explained by the stabilizing effects of carbohydrates.[66] The vesicle size distribution was analyzed by dynamic light scattering (DLS), confirming the presence of giant vesicles (Figure S2). DLS analysis showed that for the vesicles containing **DPPC-TF-H_2O_2**, 86.4% had diameters ranging from ∼1 to 20 μm, with 12.7% had an average size of 5 μm in diameter, while 76.2% of the vesicles containing **DPPC-TC-H_2S** are at an average size of 2 μm in diameter. All GUVs were freshly prepared prior to confocal imaging, treated with the redox species, and mounted directly onto a microscope slide. When incubated with the target redox species, GUVs lit up at the bilayer membrane while displaying good-to-excellent selectivity against other physiologically relevant RSS or ROS. Qualitative confocal imaging of GUVs that contain **DPPC-TC-H_2S**, POPC, POPG, and cholesterol showed a significant increase in fluorescence upon incubation

https://doi.org/10.1021/jacsau.4c00041
JACS Au 2024, 4, 1841−1853

with Na_2S (500 μM) over 1 h, while incubation with equimolar amounts of the other RSS (Cys, GSH, SO_3^{2-}, and $S_2O_3^{2-}$) reached fluorescence intensities similar to those of the untreated GUVs (Figure 4A). These observations were conceptually in line with the assays conducted under oxidative conditions: GUVs containing **DPPC-TF-H_2O_2**, POPC, POPG, and cholesterol displayed a substantial fluorescence increase at the membrane after being incubated with H_2O_2 (100 μM) over 90 min (Figure 4B). In comparison, the fluorescence intensities of those incubated with equimolar amounts of the other ROS ($^{\bullet}NO$, $^{\bullet}OH$, and $O_2^{\bullet-}$) were comparable to those for the untreated GUVs. Figure 4C provides a quantitative evaluation of fluorescence signals obtained from the membranes of multiple giant vesicles (mostly unilamellar), prepared in three independent electroformation experiments (see Figures S3 and S4 for confocal images). Collectively, these results indicated that (i) both **DPPC-TC-H_2S** and **DPPC-TF-H_2O_2** can form lipid membranes together with POPC, POPG, and cholesterol, (ii) the resulting vesicle membrane responds to a specific redox condition, displaying a high level of RSS or ROS selectivity, and (iii) the fluorescently activated redox products, **DPPC-TC** and **DPPC-TF**, remain in the membrane without disrupting it. Of note, our attempts to prepare redox-sensing GUVs from lipid compositions other than those presented here were only partially successful. Specifically, mixtures of POPC/POPG/**DPPC-TC-H_2S** (69:30:1 molar ratio) and POPC/POPG/**DPPC-TF-H_2O_2** (69.5:30:0.5 molar ratio), without cholesterol, provided GUVs (Figure S5). In contrast, we have observed a significant decrease in GUV populations when we replaced POPC with DPPC, or used mixtures of sphingomyelin and cholesterol.

Photophysical investigations on coumarin fluorophores suggest that photodimerization of two coumarin molecules is a potential mechanism for photobleaching.[67] Further, coumarin-derived fluorophores display increased photostability in nonpolar solvents.[68] Therefore, we expect that the photostability of **DPPC-TC-H_2S** and **DPPC-TC** likely increases due to their restricted molecular motions within lipid membranes as well as the nonpolar nature of these environments. Fluorescein has relatively low photostability compared to other fluorophores.[69] It has been reported that the photodegradation of fluorescein occurs within a time scale of minutes.[70] For the applications of **TEG-TF-H_2O_2** in GUVs, confocal images were captured within seconds and a decrease of fluorescein signals was not observed during the course of imaging.

MD Simulations Provide Insights into the Positioning and Conformations of Designer Lipids within Bilayer Membranes

The headgroups of both **DPPC-TC-H_2S** and **DPPC-TF-H_2O_2** contain (hetero)cyclic motifs and hydrophobic carbon extensions. In **DPPC-TC-H_2S**, phosphocholine is extended with a triazole-coumarin fluorophore caged by an azidobenzyl group. In **DPPC-TF-H_2O_2**, it is connected to a triazole-fluorescein motif with, at both of the exocyclic xanthene oxygens, a benzyl boronic acid pinacol ester. This probe design has no net charge . In comparison, the head groups of their redox reaction products, **DPPC-TC** and **DPPC-TF**, are expected to display increased hydrophilicity. Both fluorescently activated lipids should possess a higher ionic character, as their charged states will be the predominant form. Whether caged or uncaged, the headgroups of these designer phospholipid structures deviate significantly from the natural phosphocholine structure. Therefore, we sought to gain insight into their positioning within a lipid bilayer by using all-atom MD simulations. They have the resolution and dynamics necessary to describe partitioning across the heterogeneous polarity of the membrane surface. As a result, MD simulations can model to what degree probe moieties are exposed to water or the oily lipid tails.

Each designer lipid headgroup (Figures 5A and 6A) was parametrized using previously published work[71,72] and CHARMM-GUI's Ligand Reader & Modeler module,[73,74] which automatically parametrizes small molecules using the CHARMM General Force Field (CGenFF) program.[75−77] See the Supporting Information for details on the parametrization. All systems were built using scripts from CHARMM-GUI's Membrane Builder module[73,78] with one designer lipid per leaflet. The surrounding lipid matrix in each leaflet was 30 cholesterol, 48 POPC, and 21 POPG molecules, yielding a total of 100 lipids/leaflet. Net negative charge from the lipids was neutralized with K^+, and physiological salt was added into bulk water (~80 K^+, ~40 Cl^-, and 80 H_2O/lipid). For **DPPC-TC-H_2S**, **DPPC-TC**, and **DPPC-TF**, five independent replicas were constructed with the designer probes in solution. For **DPPC-TF-H_2O_2**, five independent replicas were constructed with the probe in solution, and five replicas were constructed with the probes buried in the membrane. After minimization and brief equilibration, unrestrained simulations were run using Amber22's pmemd.cuda[79−83] and the CHARMM all-atom lipid force field[84] with added parameters. All simulations were performed at 25 °C and 1 bar of pressure. All replicas of **DPPC-TC-H_2S**, **DPPC-TC**, and **DPPC-TF** were simulated 2 μs, yielding 10 μs aggregate sampling. The **DPPC-TF-H_2O_2** replicas were simulated 2.5 μs each (25 μs aggregate) to allow conformational convergence for all replicas. See the Supporting Information for details on the system build, simulation, and analysis.

Figures 5A and 6A plot the variation of the densities of the probe headgroups from the aqueous layer into the hydrophobic bilayer interior. For each probe, the triazole moieties peak between 20 and 30 Å, which is near the interface of water and the hydrophobic core (Figures 5A-left and 6A-left, violet curve; Figures 5B-left and 6B-left, violet space-filling). Interestingly, the azido group in **DPPC-TC-H_2S** was largely embedded in the hydrophobic core (Figures 5A-left, dark brown curve; and 5B-left, dark brown space-filling), which is likely a result of the overall preferred conformation of the lipid headgroup consisting of aromatic substituents (benzene, coumarin, and triazole rings). The modeled coumarin moiety of **DPPC-TC** resides in the water layer (Figure 5A-right, cyan curve; and Figure 5B-right, cyan space-filling), indicating an increase in the hydrophilicity of the headgroup following the redox reaction. Simulations of **DPPC-TF-H_2O_2** (Figure 6A-left and 6B-left) suggested that after bending at the triazole moiety near the leaflet hydrophilic/hydrophobic interface, the probe favors the hydrophobic core. Of note, this was only clear following 1.5 μs of simulation, after which all ten replicas dipped back below the surface of the leaflet. Figure S6 shows a time series of these replicas that justify dropping extensive time, allowing the probes to equilibrate. The model of **DPPC-TF** begins in water and also transiently populates a minor conformation with the xanthene moiety embedded below the interface (Figure 6A-right, bright green curves; and Figure 6B-right, bright green space-filling). Over the entire simulation, each simulated **DPPC-TF** had 1−5 conformational transitions (i.e., fully hydrated to interfacial/embedded

https://doi.org/10.1021/jacsau.4c00041
JACS Au 2024, 4, 1841−1853

conformations, vice versa), yielding ∼30 total transitions in the ensemble.

CONCLUSIONS

Artificial cells have the potential to advance life sciences, nanobiotechnology, and precision medicine.[31] One of the requirements to configure cell-like systems is to realize a mechanism for sensing. In this work, we described the design, characterization, modeling, and applications of synthetic phospholipids (**DPPC-TC-H_2S** and **DPPC-TF-H_2O_2**) that, with natural lipids, can form GUVs exhibiting activity-based sensing of redox cues. These GUVs responded to either a reductive or an oxidative condition by lighting up at the membrane, remained physically intact over the course of redox sensing, and showed good-to-excellent selectivity against nontarget redox species. The redox-sensing processes described here are irreversible, which poses a limitation for the use of GUVs in environments with a dynamic redox condition. GUV designs that allow for reversible redox sensing would be of particular interest and would likely require fluorophores that undergo redox-mediated conformational switching or chelation-induced activation.

Both **DPPC-TC-H_2S** and **DPPC-TF-H_2O_2** possess sterically bulky and hydrophobic moieties (a modified coumarin or fluorescein) attached to the phosphocholine headgroup of DPPC and, thus, display significant structural deviation from the natural phospholipids. Both the coumarin and fluorescein segments likely impose favorable hydrophobic interactions with the inner bilayer membrane. Dynamic, microsecond-scale simulations indicated that both **DPPC-TC-H_2S** and **DPPC-TF-H_2O_2** bend at the triazole moiety, inserting the bulky hydrophobic portions below the headgroup surface. We note that while the azido group in **DPPC-TC-H_2S** can be accessible to H_2S within the bilayer because the uncharged form of hydrogen sulfide permeates the membrane,[50] it may also display fast conformational dynamics in between the hydrophobic core and water/membrane interface, where it reacts with HS^-. Corresponding dynamics of the redox reaction products (**DPPC-TC** and **DPPC-TF**) indicate that the resulting phosphocholine derivatives flip, with the predominant conformations exposing the headgroup regions to water. These experimental and computational results show that our phosphocholine modifications represented at 0.5−1.0 mol % of the total lipid mixture are biophysically feasible and allow vesiculation.

This work provides a purely chemical platform for the development of lipid self-assemblies capable of sensing environmental chemical cues, one of the essential functions of artificial cells. The intrinsic chemical reactivity and self-assembling property of synthetic lipids offer new bottom-up design opportunities for laboratory models of protocells and soft materials with previously inaccessible functions.[85] We expect that future implementation of the described lipids in biological membranes could help elucidate poorly understood mechanisms by which the transient redox species affect cellular signaling.

ASSOCIATED CONTENT

Supporting Information

The Supporting Information is available free of charge at https://pubs.acs.org/doi/10.1021/jacsau.4c00041.

Chemicals; general synthetic methods; instrumental analyses; vesicle preparation and imaging; MD setup; simulation; and analysis; along with Table S1 and Figures S1−S6 (PDF)

AUTHOR INFORMATION

Corresponding Author

Enver Cagri Izgu − *Department of Chemistry and Chemical Biology, Rutgers University, New Brunswick, New Jersey 08854, United States; Cancer Institute of New Jersey, Rutgers University, New Brunswick, New Jersey 08901, United States; Rutgers Center for Lipid Research, New Jersey Institute for Food, Nutrition, and Health, Rutgers University, New Brunswick, New Jersey 08901, United States;* orcid.org/0000-0001-6673-3635; Email: ec.izgu@rutgers.edu

Authors

Huseyin Erguven − *Department of Chemistry and Chemical Biology, Rutgers University, New Brunswick, New Jersey 08854, United States;* Present Address: Paraza Pharma Inc. Montreal, Quebec, Canada

Liming Wang − *Department of Chemistry and Chemical Biology, Rutgers University, New Brunswick, New Jersey 08854, United States;* orcid.org/0000-0002-2269-5355

Bryan Gutierrez − *Department of Chemistry and Chemical Biology, Rutgers University, New Brunswick, New Jersey 08854, United States*

Andrew H. Beaven − *Unit on Membrane Chemical Physics, Eunice Kennedy Shriver National Institute of Child Health and Human Development, National Institutes of Health, Bethesda, Maryland 20892, United States; Postdoctoral Research Associate Program, National Institute of General Medical Sciences, National Institutes of Health, Bethesda, Maryland 20892, United States;* Present Address: Johnson & Johnson Innovative Medicine, Greater Philadelphia, United States

Alexander J. Sodt − *Unit on Membrane Chemical Physics, Eunice Kennedy Shriver National Institute of Child Health and Human Development, National Institutes of Health, Bethesda, Maryland 20892, United States;* orcid.org/0000-0002-5570-8212

Complete contact information is available at: https://pubs.acs.org/10.1021/jacsau.4c00041

Author Contributions

[∇]H.E. and L.W. authors contributed equally. E.C.I. conceived and oversaw the study. H.E., L.W., and B.G. conducted the experiments and acquired experimental data. A.H.B. and A.J.S. built, ran, and analyzed the MD simulations. All of the authors contributed to the interpretation of data and writing of the manuscript. CRediT: **Huseyin Erguven** data curation, formal analysis; **Liming Wang** data curation, formal analysis; **Bryan Gutierrez** data curation, formal analysis; **Andrew H. Beaven** data curation, formal analysis; **Alexander J. Sodt** formal analysis, resources, supervision; **Enver Cagri Izgu** conceptualization, formal analysis, project administration, resources, supervision, writing-original draft.

Funding

This work was supported by the Rutgers Center for Lipid Research, the American Cancer Society, Institutional Research Grant Early Investigator Award, and the Rutgers Cancer Institute of New Jersey NCI Cancer Center Support Grant

(P30CA072720) (to E.C.I.); Postdoctoral Research Associate (PRAT) fellowship from the National Institute of General Medical Sciences (1Fi2GM137844-01) (to A.H.B.); and the Intramural Research Program of the *Eunice Kennedy Shriver* National Institute of Child Health and Human Development at the National Institutes of Health (to A.H.B. and A.J.S.).

Notes

The authors declare the following competing financial interest(s): E.C.I., B.G., H.E., and L.W. are co-inventors of a provisional patent application filed by Rutgers University on the subject of this work.

■ ACKNOWLEDGMENTS

The authors thank Drs. Ralf Warmuth and Magali Rhia L. Stone for useful discussions and Dr. Gene Hall for allowing access to a fluorometer. They acknowledge Dr. Edward Castner for the donation of coumarin 343 and Dr. Jianyuan (Jason) Zhang for fluorescein. They thank Dr. Meenakshi Dutt, Dr. Akash Banerjee, and Mark J. Dresel for their interest in assisting with the early stage of the project. They acknowledge Zayna Bajwa for proofreading the manuscript and Melih Baci for assistance with mass spectrometry. This study utilized the high-performance computational capabilities of the Biowulf Linux cluster at the National Institutes of Health, Bethesda, MD (https://hpc.nih.gov).

■ ABBREVIATIONS

GUV, giant unilamellar vesicle; RSS, reactive sulfur species; ROS, reactive oxygen species; MD, molecular dynamics; DPPC, 1,2-dipalmitoyl-*rac*-glycero-3-phosphocholine; POPC, 1-palmitoyl-2-oleoyl-*sn*-glycero-3-phosphocholine; POPG, 1-palmitoyl-2-oleoyl-*sn*-glycero-3-(phosphor-*rac*-(1-glycerol)); TEG, triethylene glycol; HRMS, high-resolution mass spectrometry; LoD, limit of detection; Liss-Rhod PE, 1,2-dioleoyl-*sn*-glycero-3-phosphoethanolamine-*N*-(lissamine rhodamine B sulfonyl); Cys, cysteine; GSH, glutathione; DLS, dynamic light scattering; CGenFF, CHARMM general force field

■ REFERENCES

(1) Lyu, Y.; Peng, R.; Liu, H.; Kuai, H.; Mo, L.; Han, D.; Li, J.; Tan, W. Protocells Programmed through Artificial Reaction Networks. *Chem. Sci.* **2020**, *11* (3), 631−642.

(2) Kwiatek, J. M.; Gutierrez, B.; Izgu, E. C.; Han, G.-S.; Carman, G. M. Phosphatidic Acid Mediates the Nem1-Spo7/Pah1 Phosphatase Cascade in Yeast Lipid Synthesis. *J. Lipid Res.* **2022**, *63* (11), No. 100282.

(3) Gowland, S.; Jewett, M. C. Mobile Translation Systems Generate Genomically Engineered *Escherichia Coli* Cells with Improved Growth Phenotypes. *ACS Synth. Biol.* **2022**, *11* (9), 2969−2978.

(4) Toparlak, Ö. D.; Zasso, J.; Bridi, S.; Serra, M. D.; Macchi, P.; Conti, L.; Baudet, M.-L.; Mansy, S. S. Artificial Cells Drive Neural Differentiation. *Sci. Adv.* **2020**, *6* (38), No. eabb4920.

(5) Céspedes, P. F.; Beckers, D.; Dustin, M. L.; Sezgin, E. Model Membrane Systems to Reconstitute Immune Cell Signaling. *FEBS J.* **2021**, *288* (4), 1070−1090.

(6) Keasling, J.; Martin, H. G.; Lee, T. S.; Mukhopadhyay, A.; Singer, S. W.; Sundstrom, E. Microbial Production of Advanced Biofuels. *Nat. Rev. Microbiol* **2021**, *19* (11), 701−715.

(7) Cruz-Morales, P.; Yin, K.; Landera, A.; Cort, J. R.; Young, R. P.; Kyle, J. E.; Bertrand, R.; Iavarone, A. T.; Acharya, S.; Cowan, A.; Chen, Y.; Gin, J. W.; Scown, C. D.; Petzold, C. J.; Araujo-Barcelos, C.; Sundstrom, E.; George, A.; Liu, Y.; Klass, S.; Nava, A. A.; Keasling, J. D. Biosynthesis of Polycyclopropanated High Energy Biofuels. *Joule* **2022**, *6* (7), 1590−1605.

(8) Liu, J.; Xue, J.; Fu, L.; Xu, J.; Lord, M. S.; Liang, K. Genetically Encoded Synthetic Beta Cells for Insulin Biosynthesis and Release under Hyperglycemic Conditions. *Adv. Funct. Mater.* **2022**, *32* (18), No. 2111271.

(9) Zhao, W.; Schafer, S.; Choi, J.; Yamanaka, Y. J.; Lombardi, M. L.; Bose, S.; Carlson, A. L.; Phillips, J. A.; Teo, W.; Droujinine, I. A.; Cui, C. H.; Jain, R. K.; Lammerding, J.; Love, J. C.; Lin, C. P.; Sarkar, D.; Karnik, R.; Karp, J. M. Cell-Surface Sensors for Real-Time Probing of Cellular Environments. *Nat. Nanotechnol.* **2011**, *6* (8), 524−531.

(10) Ostrov, N.; Jimenez, M.; Billerbeck, S.; Brisbois, J.; Matragrano, J.; Ager, A.; Cornish, V. W. A Modular Yeast Biosensor for Low-Cost Point-of-Care Pathogen Detection. *Sci. Adv.* **2017**, *3* (6), No. e1603221.

(11) Vamvakaki, V.; Chaniotakis, N. A. Pesticide Detection with a Liposome-Based Nano-Biosensor. *Biosens. Bioelectron.* **2007**, *22* (12), 2848−2853.

(12) Green, D. W.; Watson, J. A.; Ben-Nissan, B.; Watson, G. S.; Stamboulis, A. Synthetic Tissue Engineering with Smart, Cytomimetic Protocells. *Biomaterials* **2021**, *276*, No. 120941.

(13) Liang, C.; Guo, B.; Wu, H.; Shao, N.; Li, D.; Liu, J.; Dang, L.; Wang, C.; Li, H.; Li, S.; Lau, W. K.; Cao, Y.; Yang, Z.; Lu, C.; He, X.; Au, D. W. T.; Pan, X.; Zhang, B.-T.; Lu, C.; Zhang, H.; Yue, K.; Qian, A.; Shang, P.; Xu, J.; Xiao, L.; Bian, Z.; Tan, W.; Liang, Z.; He, F.; Zhang, L.; Lu, A.; Zhang, G. Aptamer-Functionalized Lipid Nanoparticles Targeting Osteoblasts as a Novel RNA Interference−Based Bone Anabolic Strategy. *Nat. Med.* **2015**, *21* (3), 288−294.

(14) Manzari, M. T.; Shamay, Y.; Kiguchi, H.; Rosen, N.; Scaltriti, M.; Heller, D. A. Targeted Drug Delivery Strategies for Precision Medicines. *Nat. Rev. Mater.* **2021**, *6* (4), 351−370.

(15) Boyd, M. A.; Kamat, N. P. Designing Artificial Cells towards a New Generation of Biosensors. *Trends Biotechnol.* **2021**, *39* (9), 927−939.

(16) Kurihara, K.; Tamura, M.; Shohda, K.; Toyota, T.; Suzuki, K.; Sugawara, T. Self-Reproduction of Supramolecular Giant Vesicles Combined with the Amplification of Encapsulated DNA. *Nat. Chem.* **2011**, *3* (10), 775−781.

(17) Adamala, K. P.; Martin-Alarcon, D. A.; Guthrie-Honea, K. R.; Boyden, E. S. Engineering Genetic Circuit Interactions within and between Synthetic Minimal Cells. *Nat. Chem.* **2017**, *9* (5), 431−439.

(18) Dwidar, M.; Seike, Y.; Kobori, S.; Whitaker, C.; Matsuura, T.; Yokobayashi, Y. Programmable Artificial Cells Using Histamine-Responsive Synthetic Riboswitch. *J. Am. Chem. Soc.* **2019**, *141* (28), 11103−11114.

(19) Garamella, J.; Majumder, S.; Liu, A. P.; Noireaux, V. An Adaptive Synthetic Cell Based on Mechanosensing, Biosensing, and Inducible Gene Circuits. *ACS Synth. Biol.* **2019**, *8* (8), 1913−1920.

(20) Dupin, A.; Simmel, F. C. Signalling and Differentiation in Emulsion-Based Multi-Compartmentalized in Vitro Gene Circuits. *Nat. Chem.* **2019**, *11* (1), 32−39.

(21) Klymchenko, A. S.; Kreder, R. Fluorescent Probes for Lipid Rafts: From Model Membranes to Living Cells. *Chem. Biol.* **2014**, *21* (1), 97−113.

(22) Flores, J.; White, B. M.; Brea, R. J.; Baskin, J. M.; Devaraj, N. K. Lipids: Chemical Tools for Their Synthesis, Modification, and Analysis. *Chem. Soc. Rev.* **2020**, *49* (14), 4602−4614.

(23) Frank, J. A.; Moroni, M.; Moshourab, R.; Sumser, M.; Lewin, G. R.; Trauner, D. Photoswitchable Fatty Acids Enable Optical Control of TRPV1. *Nat. Commun.* **2015**, *6* (1), No. 7118.

(24) Mukhopadhyay, T. K.; Morstein, J.; Trauner, D. Photopharmacological Control of Cell Signaling with Photoswitchable Lipids. *Curr. Opin. Pharmacol.* **2022**, *63*, No. 102202.

(25) Chiu, D.-C.; Baskin, J. M. Imaging and Editing the Phospholipidome. *Acc. Chem. Res.* **2022**, *55* (21), 3088−3098.

(26) Farley, S.; Laguerre, A.; Schultz, C. Caged Lipids for Subcellular Manipulation. *Curr. Opin. Chem. Biol.* **2021**, *65*, 42−48.

(27) Viricel, W.; Mbarek, A.; Leblond, J. Switchable Lipids: Conformational Change for Fast PH-Triggered Cytoplasmic Delivery. *Angew. Chem., Int. Ed.* **2015**, *54* (43), 12743−12747.

https://doi.org/10.1021/jacsau.4c00041
JACS Au 2024, 4, 1841−1853

(28) Kamat, N. P.; Tobé, S.; Hill, I. T.; Szostak, J. W. Electrostatic Localization of RNA to Protocell Membranes by Cationic Hydrophobic Peptides. *Angew. Chem., Int. Ed.* **2015**, *54* (40), 11735−11739.
(29) Izgu, E. C.; Björkbom, A.; Kamat, N. P.; Lelyveld, V. S.; Zhang, W.; Jia, T. Z.; Szostak, J. W. N-Carboxyanhydride-Mediated Fatty Acylation of Amino Acids and Peptides for Functionalization of Protocell Membranes. *J. Am. Chem. Soc.* **2016**, *138* (51), 16669−16676.
(30) Lou, J.; Best, M. D. A General Approach to Enzyme-Responsive Liposomes. *Chem. −Eur. J.* **2020**, *26* (39), 8597−8607.
(31) Jiang, W.; Wu, Z.; Gao, Z.; Wan, M.; Zhou, M.; Mao, C.; Shen, J. Artificial Cells: Past, Present and Future. *ACS Nano* **2022**, *16* (10), 15705−15733.
(32) Göpfrich, K.; Platzman, I.; Spatz, J. P. Mastering Complexity: Towards Bottom-up Construction of Multifunctional Eukaryotic Synthetic Cells. *Trends Biotechnol.* **2018**, *36* (9), 938−951.
(33) Kurihara, K.; Okura, Y.; Matsuo, M.; Toyota, T.; Suzuki, K.; Sugawara, T. A Recursive Vesicle-Based Model Protocell with a Primitive Model Cell Cycle. *Nat. Commun.* **2015**, *6* (1), No. 8352.
(34) Dimova, R. Giant Vesicles and Their Use in Assays for Assessing Membrane Phase State, Curvature, Mechanics, and Electrical Properties. *Annu. Rev. Biophys.* **2019**, *48* (1), 93−119.
(35) Yuan, F.; Alimohamadi, H.; Bakka, B.; Trementozzi, A. N.; Day, K. J.; Fawzi, N. L.; Rangamani, P.; Stachowiak, J. C. Membrane Bending by Protein Phase Separation. *Proc. Natl. Acad. Sci. U.S.A.* **2021**, *118* (11), No. e2017435118.
(36) Holmström, K. M.; Finkel, T. Cellular Mechanisms and Physiological Consequences of Redox-Dependent Signalling. *Nat. Rev. Mol. Cell Bio.* **2014**, *15* (6), 411−421.
(37) Lennicke, C.; Rahn, J.; Lichtenfels, R.; Wessjohann, L. A.; Seliger, B. Hydrogen Peroxide − Production, Fate and Role in Redox Signaling of Tumor Cells. *Cell Commun. Signaling* **2015**, *13* (1), 39.
(38) Mustafa, A. K.; Gadalla, M. M.; Snyder, S. H. Signaling by Gasotransmitters. *Sci. Signaling* **2009**, *2* (68), No. re2.
(39) Sun, W.-H.; Liu, F.; Chen, Y.; Zhu, Y.-C. Hydrogen Sulfide Decreases the Levels of ROS by Inhibiting Mitochondrial Complex IV and Increasing SOD Activities in Cardiomyocytes under Ischemia/Reperfusion. *Biochem. Biophys. Res. Commun.* **2012**, *421* (2), 164−169.
(40) Olas, B. Hydrogen Sulfide as a "Double-Faced" Compound: One with Pro- and Antioxidant Effect. *Adv. Clin. Chem.* **2017**, *78*, 187−196.
(41) Sies, H. Role of Metabolic H_2O_2 Generation Redox Signaling and Oxidative Stress. *J. Biol. Chem.* **2014**, *289* (13), 8735−8741.
(42) Cheung, E. C.; Vousden, K. H. The Role of ROS in Tumour Development and Progression. *Nat. Rev. Cancer* **2022**, *22*, 280−297.
(43) Han, Y.; Shang, Q.; Yao, J.; Ji, Y. Hydrogen Sulfide: A Gaseous Signaling Molecule Modulates Tissue Homeostasis: Implications in Ophthalmic Diseases. *Cell Death Dis.* **2019**, *10* (4), 293.
(44) Sies, H.; Jones, D. P. Reactive Oxygen Species (ROS) as Pleiotropic Physiological Signalling Agents. *Nat. Rev. Mol. Cell Biol.* **2020**, *21* (7), 363−383.
(45) Kimura, H. Hydrogen Sulfide Induces Cyclic AMP and Modulates the NMDA Receptor. *Biochem. Biophys. Res. Commun.* **2000**, *267* (1), 129−133.
(46) Han, Y.; Qin, J.; Chang, X.; Yang, Z.; Bu, D.; Du, J. Modulating Effect of Hydrogen Sulfide on Gamma-Aminobutyric Acid B Receptor in Recurrent Febrile Seizures in Rats. *Neurosci. Res.* **2005**, *53* (2), 216−219.
(47) Tan, B. H.; Wong, P. T.-H.; Bian, J.-S. Hydrogen Sulfide: A Novel Signaling Molecule in the Central Nervous System. *Neurochem. Int.* **2010**, *56* (1), 3−10.
(48) Lefer, D. J. A New Gaseous Signaling Molecule Emerges: Cardioprotective Role of Hydrogen Sulfide. *Proc. Natl. Acad. Sci. U.S.A.* **2007**, *104* (46), 17907−17908.
(49) Polhemus, D. J.; Lefer, D. J. Emergence of Hydrogen Sulfide as an Endogenous Gaseous Signaling Molecule in Cardiovascular Disease. *Circ. Res.* **2014**, *114* (4), 730−737.
(50) Mathai, J. C.; Missner, A.; Kügler, P.; Saparov, S. M.; Zeidel, M. L.; Lee, J. K.; Pohl, P. No Facilitator Required for Membrane Transport of Hydrogen Sulfide. *Proc. Natl. Acad. Sci. U.S.A.* **2009**, *106* (39), 16633−16638.
(51) Cheung, E. C.; Vousden, K. H. The Role of ROS in Tumour Development and Progression. *Nat. Rev. Cancer* **2022**, *22* (5), 280−297.
(52) Bienert, G. P.; Møller, A. L. B.; Kristiansen, K. A.; Schulz, A.; Møller, I. M.; Schjoerring, J. K.; Jahn, T. P. Specific Aquaporins Facilitate the Diffusion of Hydrogen Peroxide across Membranes*. *J. Biol. Chem.* **2007**, *282* (2), 1183−1192.
(53) Bienert, G. P.; Desguin, B.; Chaumont, F.; Hols, P. Channel-Mediated Lactic Acid Transport: A Novel Function for Aquaglyceroporins in Bacteria. *Biochem. J.* **2013**, *454* (3), 559−570.
(54) Sezgin, E. Giant Plasma Membrane Vesicles to Study Plasma Membrane Structure and Dynamics. *Biochim. Biophys. Acta, Biomembr.* **2022**, *1864* (4), No. 183857.
(55) Gutierrez, B.; Aggarwal, T.; Erguven, H.; Stone, M. R. L.; Guo, C.; Bellomo, A.; Abramova, E.; Stevenson, E. R.; Laskin, D. L.; Gow, A. J.; Izgu, E. C. Direct Assessment of Nitrative Stress in Lipid Environments: Applications of a Designer Lipid-Based Biosensor for Peroxynitrite. *iScience* **2023**, *26* (12), No. 108567.
(56) Paulsen, C. E.; Carroll, K. S. Cysteine-Mediated Redox Signaling: Chemistry, Biology, and Tools for Discovery. *Chem. Rev.* **2013**, *113* (7), 4633−4679.
(57) Papapetropoulos, A.; Pyriochou, A.; Altaany, Z.; Yang, G.; Marazioti, A.; Zhou, Z.; Jeschke, M. G.; Branski, L. K.; Herndon, D. N.; Wang, R.; Szabó, C. Hydrogen Sulfide Is an Endogenous Stimulator of Angiogenesis. *Proc. Natl. Acad. Sci. U.S.A.* **2009**, *106* (51), 21972−21977.
(58) Wang, R. Physiological Implications of Hydrogen Sulfide: A Whiff Exploration That Blossomed. *Physiol. Rev.* **2012**, *92* (2), 791−896.
(59) Henthorn, H. A.; Pluth, M. D. Mechanistic Insights into the H2S-Mediated Reduction of Aryl Azides Commonly Used in H2S Detection. *J. Am. Chem. Soc.* **2015**, *137* (48), 15330−15336.
(60) Boveris, A.; Oshino, N.; Chance, B. The Cellular Production of Hydrogen Peroxide. *Biochem. J.* **1972**, *128* (3), 617−630.
(61) Dada, L. A.; Chandel, N. S.; Ridge, K. M.; Pedemonte, C.; Bertorello, A. M.; Sznajder, J. I. Hypoxia-Induced Endocytosis of Na,K-ATPase in Alveolar Epithelial Cells Is Mediated by Mitochondrial Reactive Oxygen Species and PKC-ζ. *J. Clin. Investig.* **2003**, *111*, 1057−1064.
(62) Reynolds, G. A.; Drexhage, K. H. New Coumarin Dyes with Rigidized Structure for Flashlamp-Pumped Dye Lasers. *Opt. Commun.* **1975**, *13* (3), 222−225.
(63) Kellogg, R. E.; Bennett, R. G. Radiationless Intermolecular Energy Transfer. III. Determination of Phosphorescence Efficiencies. *J. Chem. Phys.* **1964**, *41* (10), 3042−3045.
(64) Zhang, Q.; Zhu, Z.; Zheng, Y.; Cheng, J.; Zhang, N.; Long, Y.-T.; Zheng, J.; Qian, X.; Yang, Y. A Three-Channel Fluorescent Probe That Distinguishes Peroxynitrite from Hypochlorite. *J. Am. Chem. Soc.* **2012**, *134* (45), 18479−18482.
(65) Stein, H.; Spindler, S.; Bonakdar, N.; Wang, C.; Sandoghdar, V. Production of Isolated Giant Unilamellar Vesicles under High Salt Concentrations. *Front. Physiol.* **2017**, *8*, 236686.
(66) Kajii, K.; Shimomura, A.; Higashide, M. T.; Oki, M.; Tsuji, G. Effects of Sugars on Giant Unilamellar Vesicle Preparation, Fusion, PCR in Liposomes, and Pore Formation. *Langmuir* **2022**, *38* (29), 8871−8880.
(67) Karthikeyan, S.; Ramamurthy, V. Templating Photodimerization of Coumarins within a Water-Soluble Nano Reaction Vessel. *J. Org. Chem.* **2006**, *71* (17), 6409−6413.
(68) Jivaramonaikul, W.; Rashatasakhon, P.; Wanichwecharungruang, S. UVA Absorption and Photostability of Coumarins. *Photochem. Photobiol. Sci.* **2010**, *9* (8), 1120−1125.
(69) Hinkeldey, B.; Schmitt, A.; Jung, G. Comparative Photostability Studies of BODIPY and Fluorescein Dyes by Using Fluorescence Correlation Spectroscopy. *ChemPhysChem* **2008**, *9* (14), 2019−2027.
(70) Bojinov, V. B.; Panova, I. P.; Simeonov, D. B. The Synthesis of Novel Photostable Fluorescein-Based Dyes Containing an s-Triazine UV Absorber and a HALS Unit and Their Acrylonitrile Copolymers. *Dyes Pigm.* **2009**, *83* (2), 135−143.

https://doi.org/10.1021/jacsau.4c00041
JACS Au 2024, 4, 1841−1853

(71) Mayne, C. G.; Saam, J.; Schulten, K.; Tajkhorshid, E.; Gumbart, J. C. Rapid Parameterization of Small Molecules Using the Force Field Toolkit. *J. Comput. Chem.* **2013**, *34* (32), 2757−2770.
(72) Smith, A. K.; Wilkerson, J. W.; Knotts, T. A. Parameterization of Unnatural Amino Acids with Azido and Alkynyl R-Groups for Use in Molecular Simulations. *J. Phys. Chem. A* **2020**, *124* (30), 6246−6253.
(73) Jo, S.; Kim, T.; Iyer, V. G.; Im, W. CHARMM-GUI: A Web-based Graphical User Interface for CHARMM. *J. Comput. Chem.* **2008**, *29* (11), 1859−1865.
(74) Kim, S.; Lee, J.; Jo, S.; Brooks, C. L.; Lee, H. S.; Im, W. CHARMM-GUI Ligand Reader and Modeler for CHARMM Force Field Generation of Small Molecules. *J. Comput. Chem.* **2017**, *38* (21), 1879−1886.
(75) Vanommeslaeghe, K.; Hatcher, E.; Acharya, C.; Kundu, S.; Zhong, S.; Shim, J.; Darian, E.; Guvench, O.; Lopes, P.; Vorobyov, I.; Mackerell, A. D. CHARMM General Force Field: A Force Field for Drug-like Molecules Compatible with the CHARMM All-atom Additive Biological Force Fields. *J. Comput. Chem.* **2010**, *31* (4), 671−690.
(76) Vanommeslaeghe, K.; MacKerell, A. D. Automation of the CHARMM General Force Field (CGenFF) I: Bond Perception and Atom Typing. *J. Chem. Inf. Model.* **2012**, *52* (12), 3144−3154.
(77) Vanommeslaeghe, K.; Raman, E. P.; MacKerell, A. D. Automation of the CHARMM General Force Field (CGenFF) II: Assignment of Bonded Parameters and Partial Atomic Charges. *J. Chem. Inf. Model.* **2012**, *52* (12), 3155−3168.
(78) Lee, J.; Cheng, X.; Swails, J. M.; Yeom, M. S.; Eastman, P. K.; Lemkul, J. A.; Wei, S.; Buckner, J.; Jeong, J. C.; Qi, Y.; Jo, S.; Pande, V. S.; Case, D. A.; Brooks, C. L.; MacKerell, A. D.; Klauda, J. B.; Im, W. CHARMM-GUI Input Generator for NAMD, GROMACS, AMBER, OpenMM, and CHARMM/OpenMM Simulations Using the CHARMM36 Additive Force Field. *J. Chem. Theory Comput.* **2016**, *12* (1), 405−413.
(79) Case, D. A.; Cheatham, T. E.; Darden, T.; Gohlke, H.; Luo, R.; Merz, K. M.; Onufriev, A.; Simmerling, C.; Wang, B.; Woods, R. J. The Amber Biomolecular Simulation Programs. *J. Comput. Chem.* **2005**, *26* (16), 1668−1688.
(80) Case, D. A.; Aktulga, H. M.; Belfon, K.; Ben-Shalom, I. Y.; Berryman, J. T.; Brozell, S. R.; Cerutti, D. S.; Cheatham, T. E., III; Cisneros, G. A.; Cruzeiro, V. W. D.; Darden, T. A.; Forouzesh, N.; Giambaşu, G.; Giese, T.; Gilson, M. K.; Gohlke, H.; Goetz, A. W.; Harris, J.; Izadi, S.; Izmailov, S. A.; Kasavajhala, K.; Kaymak, M. C.; King, E.; Kovalenko, A.; Kurtzman, T.; Lee, T. S.; Li, P.; Lin, C.; Liu, J.; Luchko, T.; Luo, R.; Machado, M.; Man, V.; Manathunga, M.; Merz, K. M.; Miao, Y.; Mikhailovskii, O.; Monard, G.; Nguyen, H.; O'Hearn, K. A.; Onufriev, A.; Pan, F.; Pantano, S.; Qi, R.; Rahnamoun, A.; Roe, D. R.; Roitberg, A.; Sagui, C.; Schott-Verdugo, S.; Shajan, A.; Shen, J.; Simmerling, C. L.; Skrynnikov, N. R.; Smith, J.; Swails, J.; Walker, R. C.; Wang, J.; Wang, J.; Wei, H.; Wu, X.; Wu, Y.; Xiong, Y.; Xue, Y.; York, D. M.; Zhao, S.; Zhu, Q.; Kollman; Amber, P. A. University of California: San Francisco, 2023.
(81) Götz, A. W.; Williamson, M. J.; Xu, D.; Poole, D.; Grand, S. L.; Walker, R. C. Routine Microsecond Molecular Dynamics Simulations with AMBER on GPUs. 1. Generalized Born. *J. Chem. Theory Comput.* **2012**, *8* (5), 1542−1555.
(82) Salomon-Ferrer, R.; Götz, A. W.; Poole, D.; Grand, S. L.; Walker, R. C. Routine Microsecond Molecular Dynamics Simulations with AMBER on GPUs. 2. Explicit Solvent Particle Mesh Ewald. *J. Chem. Theory Comput.* **2013**, *9* (9), 3878−3888.
(83) Le Grand, S.; Götz, A. W.; Walker, R. C. SPFP: Speed without Compromise−A Mixed Precision Model for GPU Accelerated Molecular Dynamics Simulations. *Comput. Phys. Commun.* **2013**, *184* (2), 374−380.
(84) Klauda, J. B.; Venable, R. M.; Freites, J. A.; O'Connor, J. W.; Tobias, D. J.; Mondragon-Ramirez, C.; Vorobyov, I.; MacKerell, A. D.; Pastor, R. W. Update of the CHARMM All-Atom Additive Force Field for Lipids: Validation on Six Lipid Types. *J. Phys. Chem. B* **2010**, *114* (23), 7830−7843.
(85) Liu, Z.; Zhou, W.; Qi, C.; Kong, T. Interface Engineering in Multiphase Systems toward Synthetic Cells and Organelles: From Soft Matter Fundamentals to Biomedical Applications. *Adv. Mater.* **2020**, *32* (43), No. e2002932.

https://doi.org/10.1021/jacsau.4c00041
JACS Au 2024, 4, 1841−1853